Supporting Information

Mesoporous Mn-Fe oxyhydroxides for oxygen evolution

Jingyi Han,[a,†] Mingzhu Zhang,[b,†] Xue Bai,[a] Zhiyao Duan,[b,*] Tianmi Tang,[a] and Jingqi

Guan[a,*]

[a] Institute of Physical Chemistry, College of Chemistry, Jilin University, 2519 Jiefang

Road, Changchun 130021, P.R. China. *E-mail: guanjq@jlu.edu.cn

[b] State Key Laboratory of Solidification Processing, School of Materials Science and

Engineering, Northwestern Polytechnical University, Xi'an 710072, P. R. China, *E-

mail: zhiyao.duan@nwpu.edu.cn

[†]These authors contributed equally to this work.

Synthesis of Meso-Mn$_1$Fe$_n$O$_x$

Meso-Mn$_1$Fe$_n$O$_x$ with different Fe/Mn ratios were synthesized via a facile co-

precipitation route. Firstly, 0.5 g polyethylene oxide–polypropylene oxide–

polyethylene oxide (P123) was dissolved in 50 ml deionized water (DW). Then,

MnCl$_2$·4H$_2$O (1 mmol) and FeCl$_3$ (0.4 - 1.2 mmol) were added to the above solution

under stirring. Afterwards, Na$_2$CO$_3$ solution was slowly added. When the reaction was

complete, the mixture was filtered and washed with DW and ethanol. Finally, the

obtained precursor was dried at 35 °C for 12 h to obtain Meso-$Mn_1Fe_nO_x$. For comparison, Meso-MnO_x and Meso-FeO_x were synthesized following a process similar to that for Meso-$Mn_1Fe_nO_x$.

Characterization

Transmission electron microscope (TEM) images were observed by a HITACHI HT7700. High-resolution TEM (HRTEM) images were recorded on a JEM-2100 transmission electron microscope (Tokyo, Japan) at 200 kV. SEM images were recorded on a HITACHI SU8020 field emission scanning electron microscope. The valence state was determined using XPS recorded on a Thermo ESCALAB 250Xi. The X-ray source selected was monochromatized Al Kα source (15 kV, 10.8 mA). Region scans were collected using a 30 eV pass energy. Peak positions were calibrated relative to C 1s peak position at 284.6 eV.

Electrochemical measurements

All electrochemical measurements were performed on a CHI760E electrochemical working station at room temperature. The catalysts were measured in 1.0 M KOH aqueous solution using a typical three-electrode configuration, in which glassy carbon electrode (GCE) was used as the working electrode; platinum plate and saturated calomel electrode (SCE, saturated KCl) were used as the counter and reference electrodes, respectively. Linear sweep voltammetry (LSV) polarization curves were acquired at a scan rate of 1 mV·s^{-1}

with 90% *i*R-compensation. Electrochemical impedance spectroscopy (EIS) measurements were performed at open-circuit potential in the frequency range from 100 kHz to 0.1 Hz with an a.c. perturbation of 5 mV. All potentials measured were calibrated to RHE using the following equation: E (versus RHE) = E (versus SCE) + 0.241 V + 0.0591 pH.

Computational methods

Spin-polarized DFT calculations were performed using the Vienna Ab initio Simulation Package.[1, 2] The generalized gradient approximation with the PBE functional[3] was used to describe the exchange and correlation energy. Electron−ion interactions were treated by the projector augmented wave method.[4] In all calculations, the energy cutoff of the plane-wave basis set was 400 eV. DFT+U method was applied to 3*d* orbitals of Fe and Co to correct the on site Coulomb interactions.[5] U_{eff} = 5 eV were used for both Fe and Mn to reproduce the electronic structure that has been observed experimentally.[6] Brillouin zone was sampled by Monkhorst-Pack k-point meshes.[7] Optimized structures were obtained by minimizing the forces on each ion until they fell below 0.05 eV/Å. The solvation effects were also considered using an implicit solvation model implemented in VASP.[8] The relative permittivity for the continuum solvent was set to 80 to simulate a water environment. The OER activities of various active sites are evaluated using the computational hydrogen electrode method.[9]
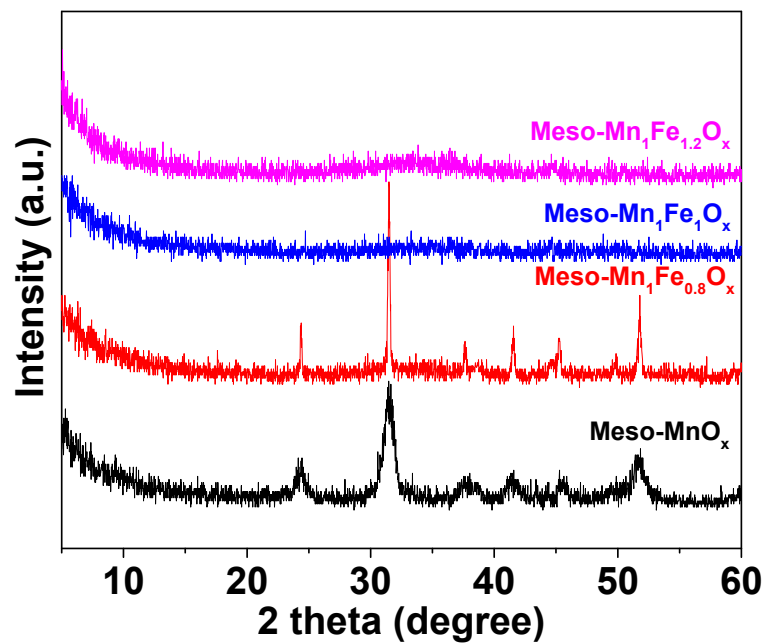
Figure S1. XRD patterns of Meso-MnO$_x$, Meso-Mn$_1$Fe$_{0.8}$O$_x$, Meso-Mn$_1$Fe$_1$O$_x$, and Meso-Mn$_1$Fe$_{1.2}$O$_x$.
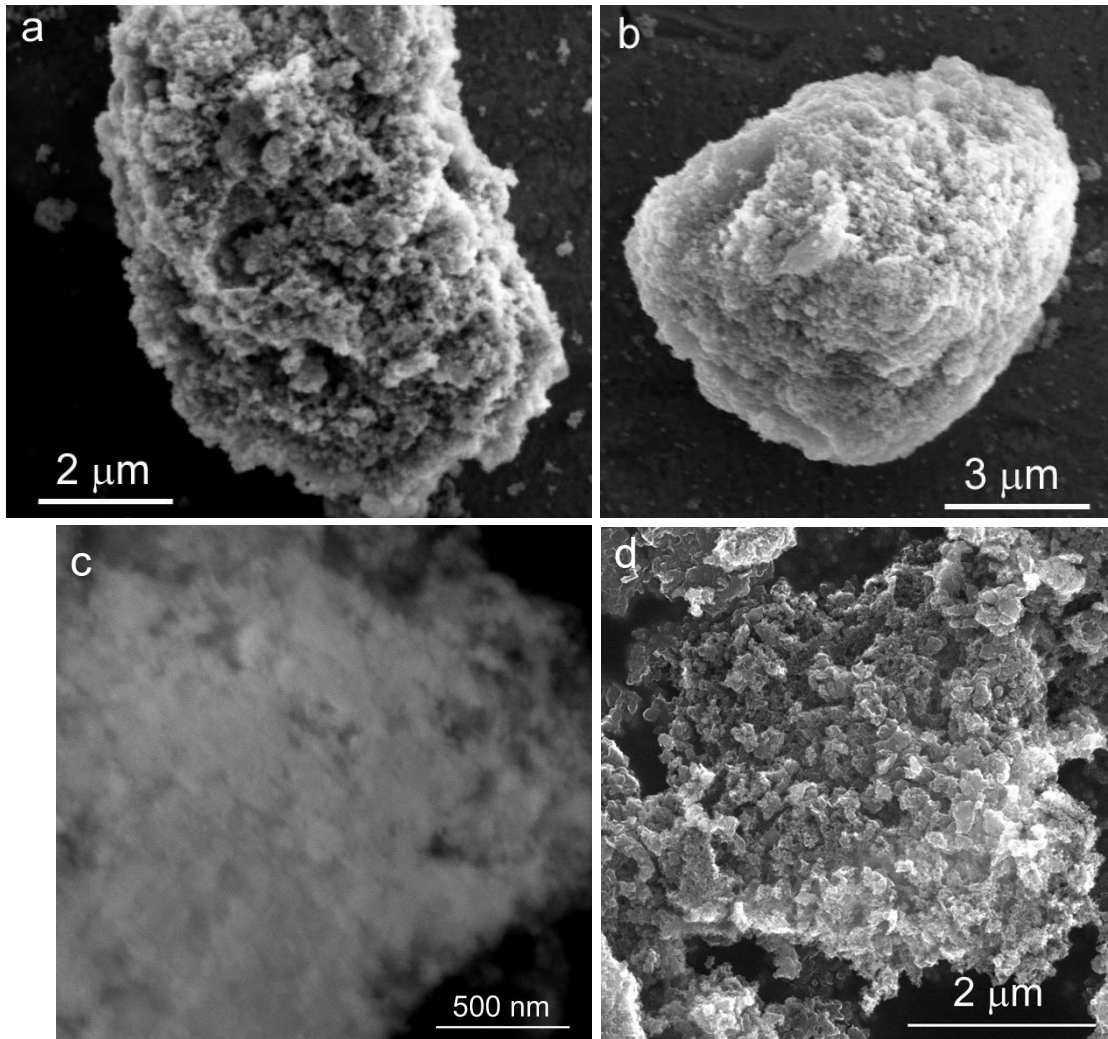
Figure S2. SEM images of (a) Meso-$Mn_1Fe_{0.8}O_x$, (b) Meso-$Mn_1Fe_{1.2}O_x$, (c) FeO_x and
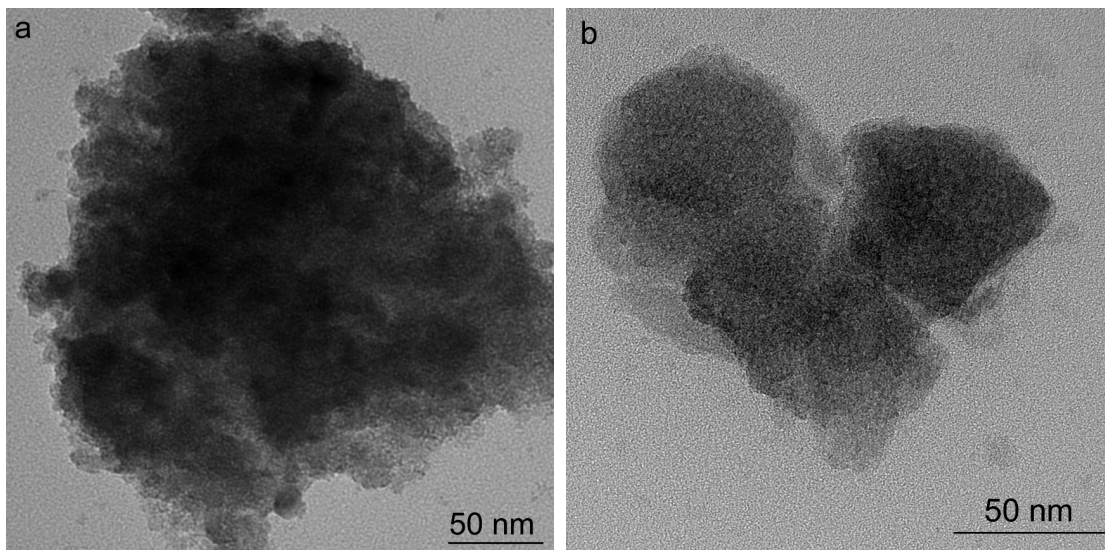
(d) MnO_x.

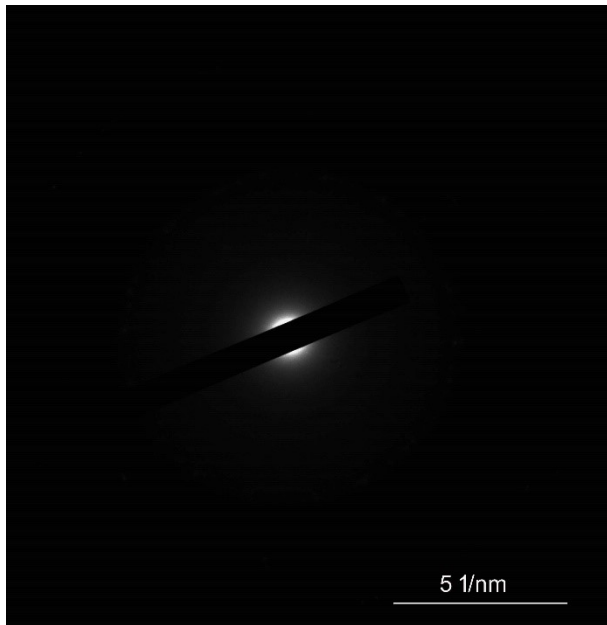**Figure S3.** TEM images of (a) FeO$_x$ and (b) MnO$_x$.

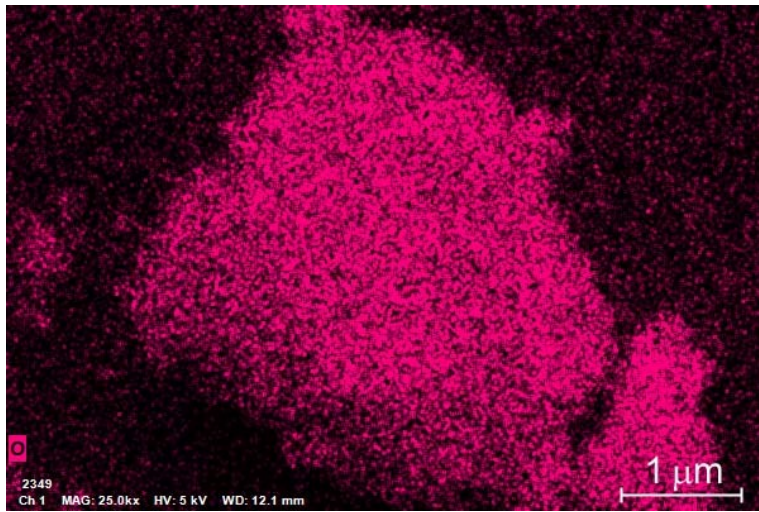**Figure S4.** SAED pattern of Meso-$Mn_1Fe_1O_x$.
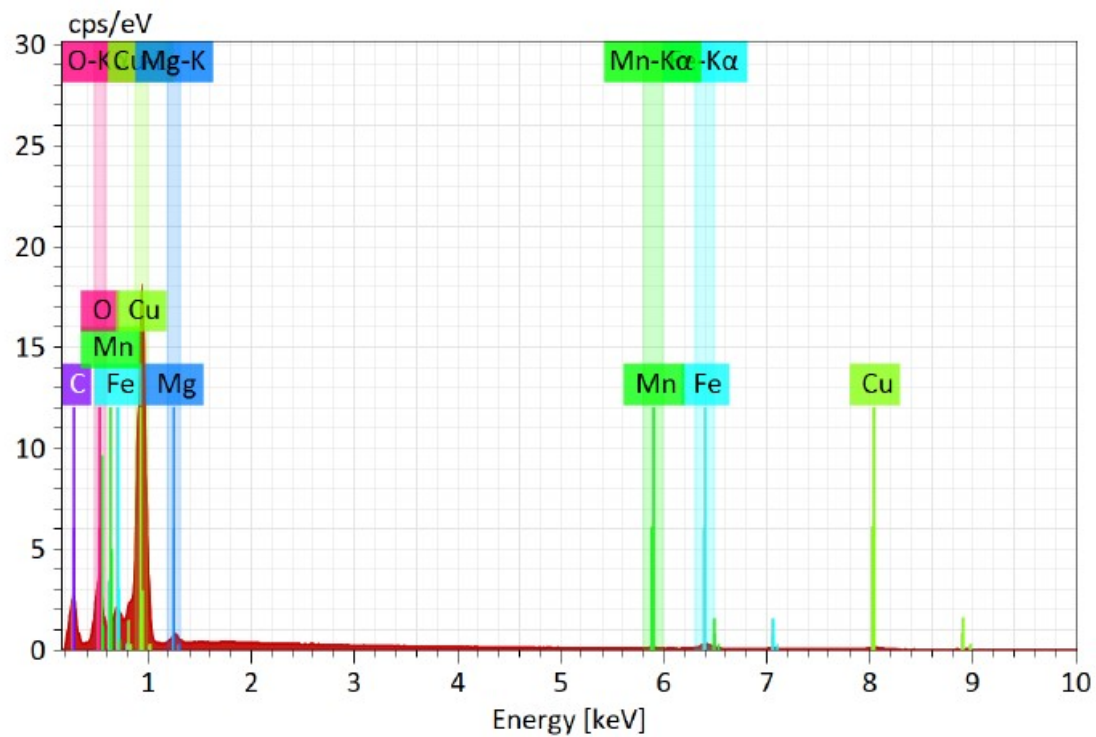
Figure S5. Element mapping of O.

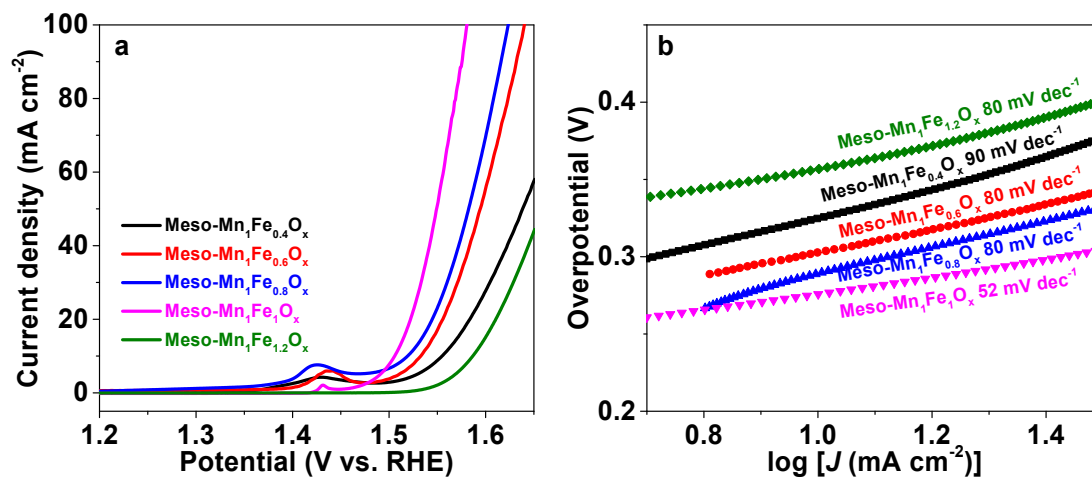**Figure S6.** SEM-EDS of the Meso-$Mn_1Fe_1O_x$ supported on copper grid.

Figure S7. (a) OER polarization curves of Meso-$Mn_1Fe_nO_x$. (b) Tafel slopes.
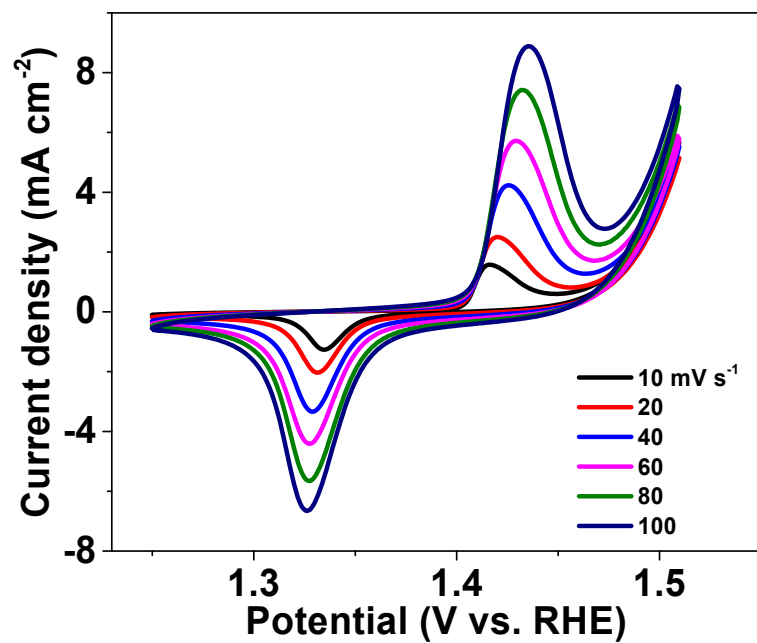
Figure S8. CV of Meso-$Mn_1Fe_1O_x$ in 1 M KOH at scan rates of 10–100 mV s^{-1}.
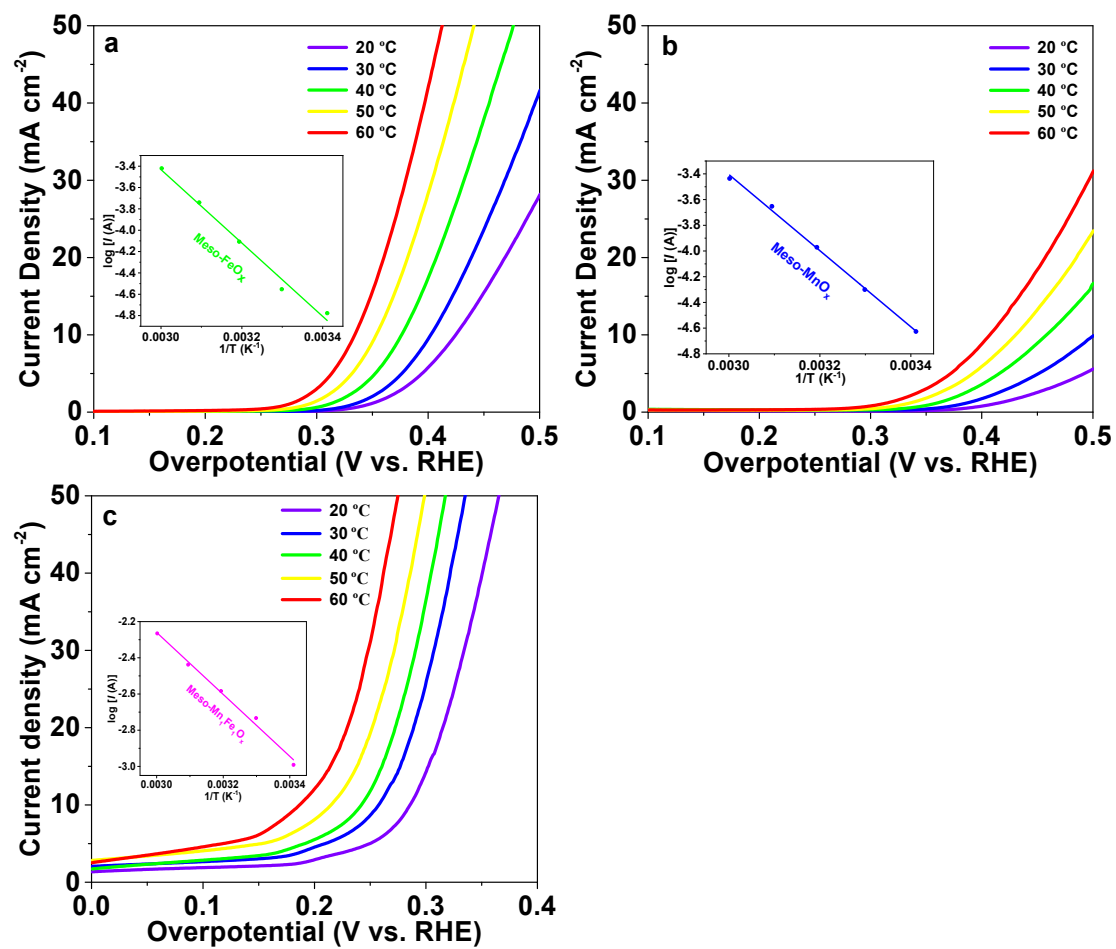
Figure S9. OER polarization curves of (a) Meso-FeO$_x$, (b) Meso-MnO$_x$, and (c) Meso-Mn$_1$Fe$_1$O$_x$ in three-electrode configuration in 1 M KOH at 20 °C, 30 °C, 40 °C, 50 °C, and 60 °C.
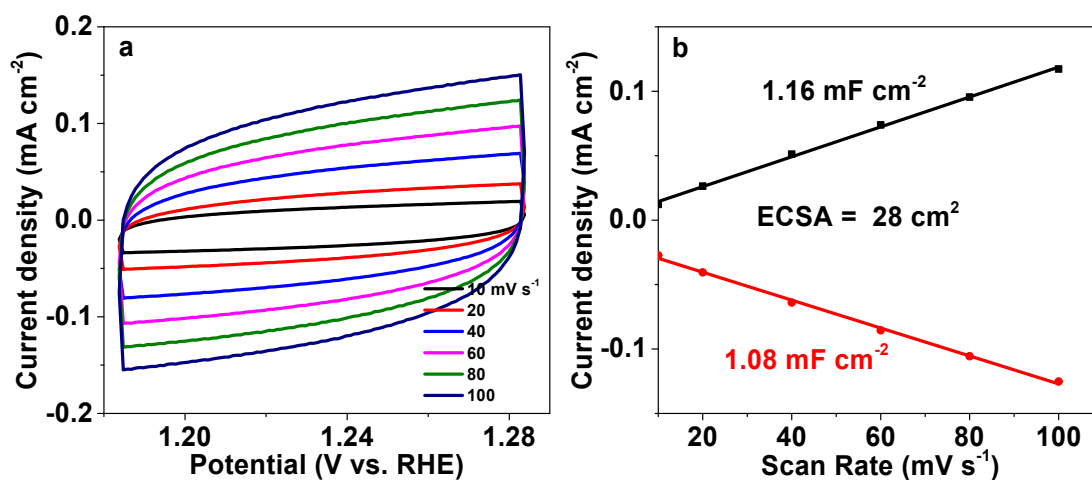
Figure S10. (a) CVs of Meso-FeO$_x$ measured in a non-Faradaic region at scan rate of 20 mV s^{-1}, 40 mV s^{-1}, 60 mV s^{-1}, 80 mV s^{-1}, and 100 mV s^{-1}. (b) The cathodic (black) and anodic (red) currents measured at 1.234 V vs RHE as a function of the scan rate. The average of the absolute value of the slope is taken as the double-layer capacitance of the electrode.
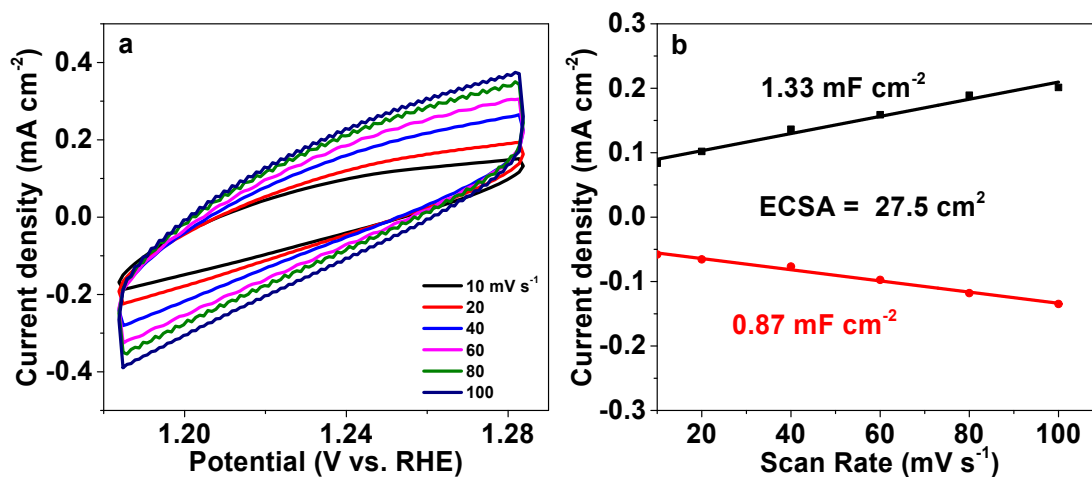
Figure S11. (a) CVs of Meso-MnO$_x$ measured in a non-Faradaic region at scan rate of 20 mV s^{-1}, 40 mV s^{-1}, 60 mV s^{-1}, 80 mV s^{-1}, and 100 mV s^{-1}. (b) The cathodic (black) and anodic (red) currents measured at 1.234 V vs RHE as a function of the scan rate. The average of the absolute value of the slope is taken as the double-layer capacitance of the electrode.

Figure S12. (a) CVs of Meso-$Mn_1Fe_1O_x$ measured in a non-Faradaic region at scan rate of 20 mV s^{-1}, 40 mV s^{-1}, 60 mV s^{-1}, 80 mV s^{-1}, and 100 mV s^{-1}. (b) The cathodic (black) and anodic (red) currents measured at 1.234 V vs RHE as a function of the scan rate. The average of the absolute value of the slope is taken as the double-layer capacitance of the electrode.
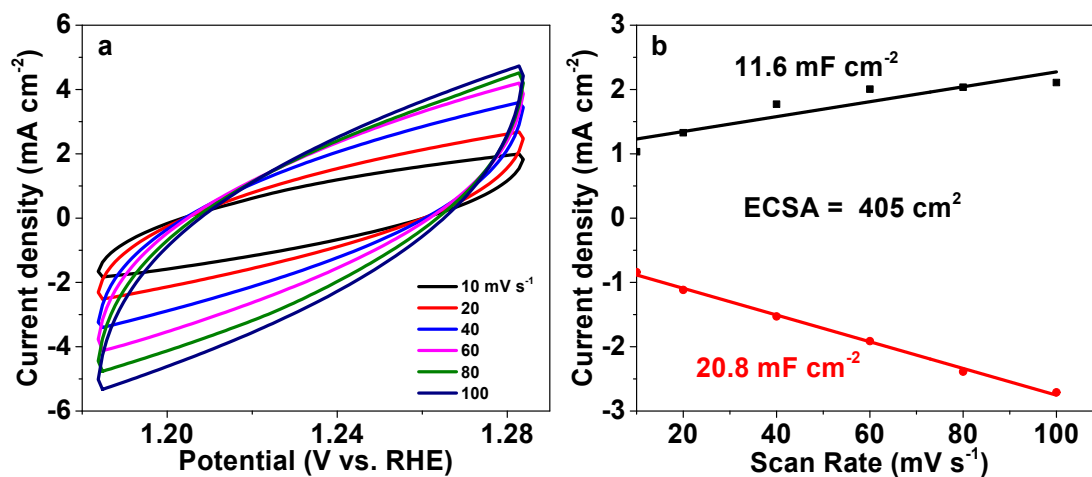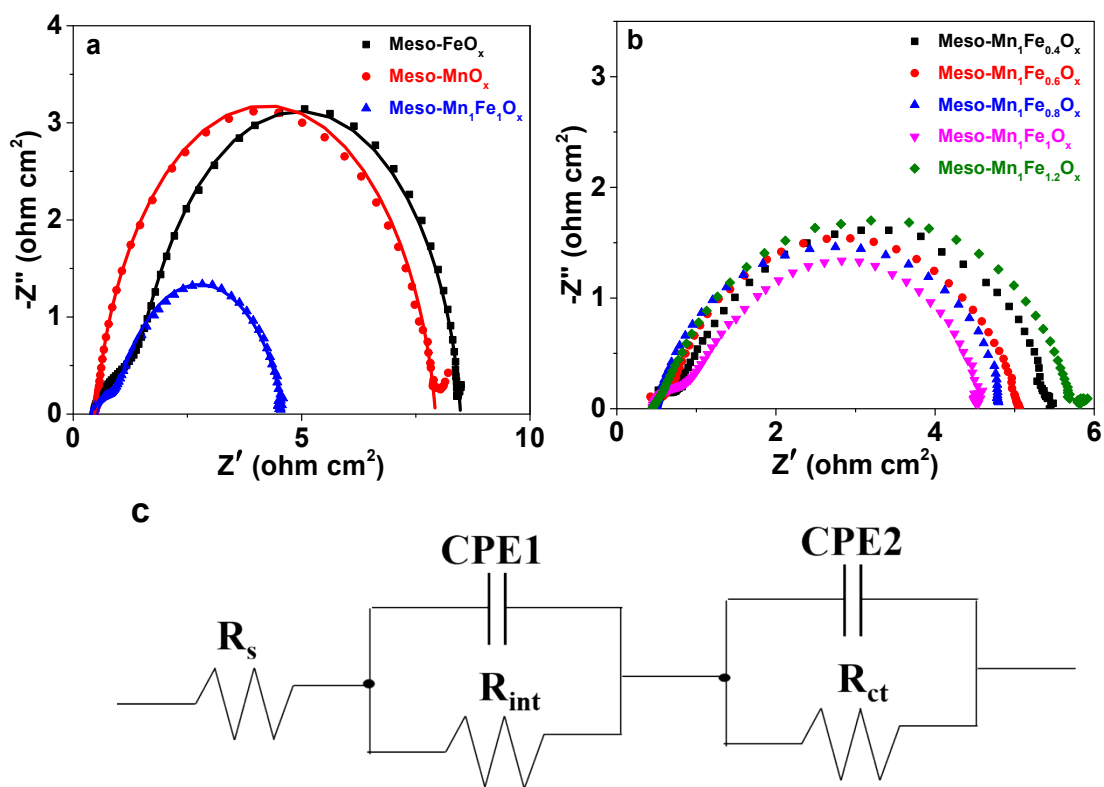
Figure S13. (a) Nyquist plots of the EIS test for Meso-FeO$_x$, Meso-MnO$_x$, and Meso-Mn$_1$Fe$_1$O$_x$. (b) Nyquist plots of the EIS test for Meso-Mn$_1$Fe$_n$O$_x$. (c) The equivalent circuit used for fitting the Nyquist plots. R$_s$, R$_{ct}$ and R$_{int}$ represent the series resistance, charge-transfer resistance and solid-electrolyte interface resistance, respectively; and the parameters of CPE1 and CPE2 correspond to the double-layer capacitance and the Faradic capacitance, respectively.

Figure S14. XRD pattern of the used $Mn_1Fe_1O_x$.

Figure S15. TEM image of the used $Mn_1Fe_1O_x$.

Figure S16. (a) SEM image and (b) EDS spectrum of the used $Mn_1Fe_1O_x$ supported on copper grid.
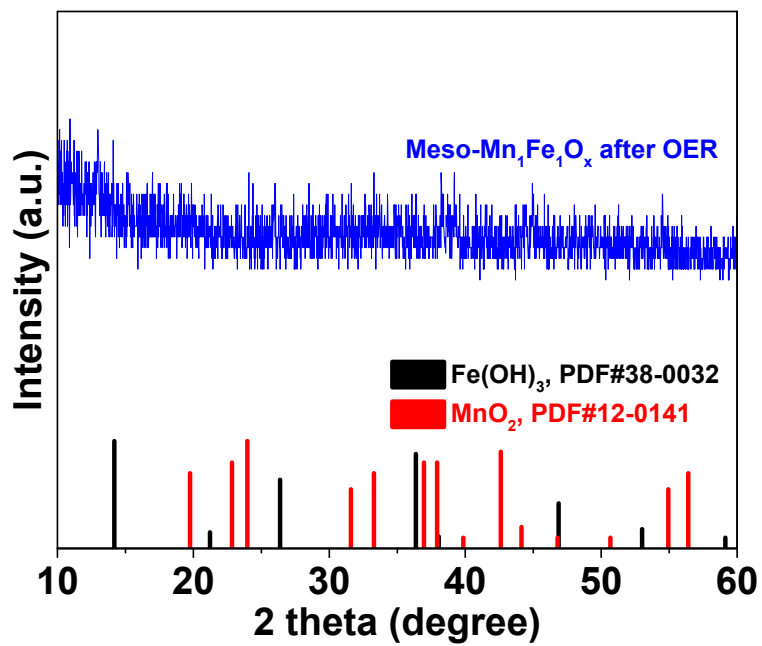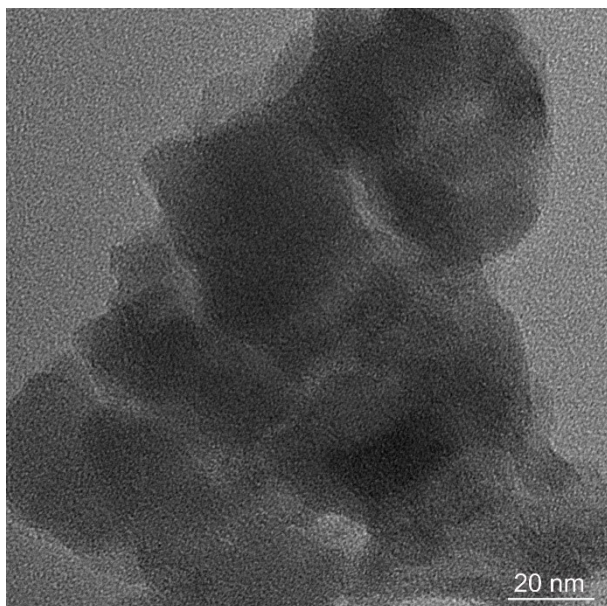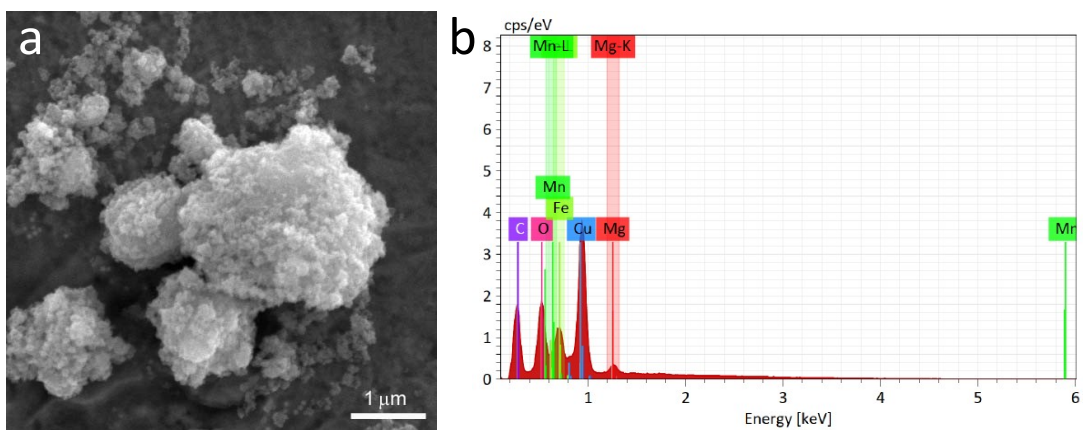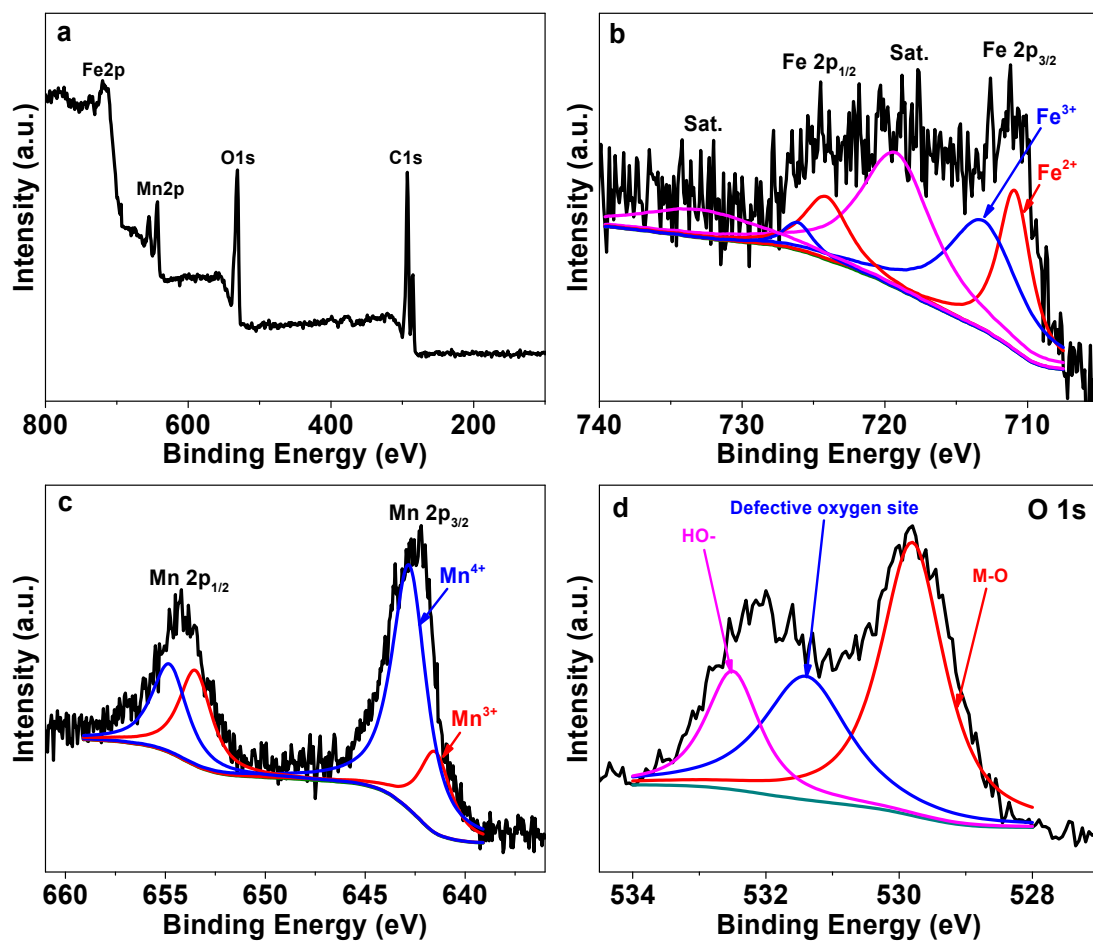
Figure S17. (a) XPS survey spectrum of the used $Mn_1Fe_1O_x$. (b) High-resolution Fe 2p XPS spectrum. (c) High-resolution Mn 2p XPS spectrum. (d) High-resolution O 1s XPS spectrum.

Table S1 Comparison of OER performance of Meso-$Mn_1Fe_1O_x$ with other MnFe-based catalysts in 1.0 M KOH

catalyst	η @ 10mA cm^{-2} (mV)	Tafel slope (mV dec^{-1})	Ref.
Meso-$Mn_1Fe_1O_x$	275	52	This work
Mn-Fe oxide/CC	730	80	[10]
$Mn_{0.5}Fe_{2.5}O_4$NP/MC	560	129	[11]
$MnFe_2O_4$NP/MC	510	88	[11]
Fe/Mn-N-C	360	60	[12]
$Fe_{1.1}Mn_{0.9}P$	440	62	[13]
$MnFe_2O_4$/NF	310	65	[14]
$MnFe_2O_4$	582	71	[15]
Fe–Mn–O NS/CC	273	63.9	[16]
$Mn-Fe_2O_3$	351	102	[17]
a-Fe-Mn:Pi	252	52	[18]
α-$Mn_{1-x}Fe_xO_2$	400	59	[19]
$Mn_{0.5}(Fe_{0.3}Ni_{0.7})_{0.5}$	340	-	[20]
Fe_2O_3-MnO/NF	370	66	[21]
Mn-FeOOH/FTO	246	71	[22]
Fe-MnSe/NF	247	35	[23]
Mn@HUST-8	485	240.8	[24]
P-$FeMnO_x$	251	-	[25]

References

1. Kresse and Hafner, Ab initio molecular dynamics for liquid metals, *Physical review. B, Condensed matter*, 1993, **47**, 558-561.

2. Kresse and Furthmuller, Efficient iterative schemes for ab initio total-energy calculations using a plane-wave basis set, *Physical review. B, Condensed matter*, 1996, **54**, 11169-11186.

3. Perdew, Burke and Ernzerhof, Generalized gradient approximation made simple, *Phys. Rev. Lett.*, 1996, **77**, 3865-3868.

4. Blochl, Projector augmented-wave method, *Physical review. B, Condensed matter*, 1994, **50**, 17953-17979.

5. S. L. Dudarev, G. A. Botton, S. Y. Savrasov, C. J. Humphreys and A. P. Sutton, Electron-energy-loss spectra and the structural stability of nickel oxide: An LSDA+U study, *Physical Review B*, 1998, **57**, 1505-1509.

6. A. Rohrbach, J. Hafner and G. Kresse, Ab initio study of the (0001) surfaces of hematite and chromia: Influence of strong electronic correlations, *Physical Review B*, 2004, **70**.

7. Froyen, Brillouin-zone integration by Fourier quadrature: Special points for superlattice and supercell calculations, *Physical review. B, Condensed matter*, 1989, **39**, 3168-3172.

8. K. Mathew, R. Sundararaman, K. Letchworth-Weaver, T. A. Arias and R. G. Hennig, Implicit solvation model for density-functional study of nanocrystal

surfaces and reaction pathways, *J. Chem. Phys.*, 2014, **140**.

9.   J. K. Nørskov, J. Rossmeisl, A. Logadottir, L. Lindqvist, J. R. Kitchin, T. Bligaard and H. Jónsson, Origin of the Overpotential for Oxygen Reduction at a Fuel-Cell Cathode, *J. Phys. Chem. B*, 2004, **108**, 17886-17892.

10.   N. Bhandary, P. P. Ingole and S. Basu, Electrosynthesis of Mn-Fe oxide nanopetals on carbon paper as bi-functional electrocatalyst for oxygen reduction and oxygen evolution reaction, *Int. J. Hydrogen Energy*, 2018, **43**, 3165-3171.

11.   Y. Konno, T. Yamamoto and T. Nagayama, Nanoporous manganese ferrite films by anodising electroplated Fe-Mn alloys for bifunctional oxygen electrodes, *Nanoscale*, 2021, **13**, 12738-12749.

12.   X. Wu, Y. Niu, B. Feng, Y. Yu, X. Huang, C. Zhong, W. Hu and C. M. Li, Mesoporous Hollow Nitrogen-Doped Carbon Nanospheres with Embedded MnFe2O4/Fe Hybrid Nanoparticles as Efficient Bifunctional Oxygen Electrocatalysts in Alkaline Media, *ACS Appl Mater Interfaces*, 2018, **10**, 20440-20447.

13.   D. Li, H. Baydoun, B. Kulikowski and S. L. Brock, Boosting the Catalytic Performance of Iron Phosphide Nanorods for the Oxygen Evolution Reaction by Incorporation of Manganese, *Chem. Mater.*, 2017, **29**, 3048-3054.

14.   M. Li, Y. Xiong, X. Liu, X. Bo, Y. Zhang, C. Han and L. Guo, Facile synthesis of electrospun MFe2O4 (M = Co, Ni, Cu, Mn) spinel nanofibers with excellent electrocatalytic properties for oxygen evolution and hydrogen peroxide reduction, *Nanoscale*, 2015, **7**, 8920-8930.

15. C. Si, Y. Zhang, C. Zhang, H. Gao, W. Ma, L. Lv and Z. Zhang, Mesoporous nanostructured spinel-type MFe2O4 (M = Co, Mn, Ni) oxides as efficient bi-functional electrocatalysts towards oxygen reduction and oxygen evolution, *Electrochim. Acta*, 2017, **245**, 829-838.

16. Y. Teng, X.-D. Wang, J.-F. Liao, W.-G. Li, H.-Y. Chen, Y.-J. Dong and D.-B. Kuang, Atomically Thin Defect-Rich Fe-Mn-O Hybrid Nanosheets as High Efficient Electrocatalyst for Water Oxidation, *Adv. Funct. Mater.*, 2018, **28**.

17. M. S. Burke, L. J. Enman, A. S. Batchellor, S. Zou and S. W. Boettcher, Oxygen Evolution Reaction Electrocatalysis on Transition Metal Oxides and (Oxy)hydroxides: Activity Trends and Design Principles, *Chem. Mater.*, 2015, **27**, 7549-7558.

18. Y. Liu, J. Zhang, W. Wang, L. Cao and B. Dong, Two-Phase Colloidal Synthesis of Amorphous Iron-Doped Manganese Phosphate Hollow Nanospheres for Efficient Water Oxidation, *Adv. Sustainable Syst.*, 2020, **4**.

19. J. M. Lee, S. B. Patil, B. Kang, S. Lee, M. G. Kim and S.-J. Hwang, Understanding the crucial role of local crystal order in the electrocatalytic activity of crystalline manganese oxide, *J. Mater. Chem. A*, 2018, **6**, 12565-12573.

20. D. M. Morales, M. A. Kazakova, S. Dieckhöfer, A. G. Selyutin, G. V. Golubtsov, W. Schuhmann and J. Masa, Trimetallic Mn-Fe-Ni Oxide Nanoparticles Supported on Multi-Walled Carbon Nanotubes as High-Performance Bifunctional ORR/OER Electrocatalyst in Alkaline Media,

Adv. Funct. Mater., 2019, **30**.

21. J. Kim, J. N. Heo, J. Y. Do, R. K. Chava and M. Kang, Electrochemical Synergies of Heterostructured Fe2O3-MnO Catalyst for Oxygen Evolution Reaction in Alkaline Water Splitting, *Nanomaterials (Basel)*, 2019, **9**.

22. M. P. Suryawanshi, U. V. Ghorpade, S. W. Shin, U. P. Suryawanshi, H. J. Shim, S. H. Kang and J. H. Kim, Facile, Room Temperature, Electroless Deposited (Fe1-x, Mnx)OOH Nanosheets as Advanced Catalysts: The Role of Mn Incorporation, *Small*, 2018, **14**, e1801226.

23. M. Sun, R.-T. Gao, X. Liu, R. Gao and L. Wang, Manganese-based oxygen evolution catalysts boosting stable solar-driven water splitting: MnSe as an intermetallic phase, *J. Mater. Chem. A*, 2020, **8**, 25298-25305.

24. R.-L. Peng, J.-L. Li, X.-N. Wang, Y.-M. Zhao, B. Li, B. Y. Xia and H.-C. Zhou, Single-atom implanted two-dimensional MOFs as efficient electrocatalysts for the oxygen evolution reaction, *Inorg. Chem. Front.*, 2020, **7**, 4661-4668.

25. L. Shen, Q. Zhang, J. Luo, H. C. Fu, X. H. Chen, L. L. Wu, H. Q. Luo and N. B. Li, Heteroatoms Adjusting Amorphous FeMn-Based Nanosheets via a Facile Electrodeposition Method for Full Water Splitting, *ACS Sustainable Chem. Eng.*, 2021, **9**, 5963-5971.